All-Silicon Broadband Ultraviolet Metasurfaces

Yang Deng, Xi Wang, Zilun Gong, Kaichen Dong, Shuai Lou, Nicolas Pégard, Kyle B. Tom, Fuyi Yang, Zheng You, Laura Waller, and Jie Yao*

Featuring high photon energy and short wavelength, ultraviolet (UV) light enables numerous applications such as high-resolution imaging, photolithography, and sensing. In order to manipulate UV light, bulky optics are usually required, and hence do not meet the fast-growing requirements of integration in compact systems. Recently, metasurfaces have shown unprecedented control of light, enabling substantial miniaturization of photonic devices from terahertz to visible regions. However, material challenges have hampered the realization of such functionalities at shorter wavelengths. Herein, it is experimentally demonstrated that all-silicon (Si) metasurfaces with thicknesses of only one-tenth of the working wavelength can be designed and fabricated to manipulate broadband UV light with efficiencies comparable to plasmonic metasurface performance in infrared (IR). Also, for the first time, photolithography enabled by metasurface-generated UV holograms is shown. Such performance enhancement is attributed to increased scattering cross sections of Si antennas in the UV range, which is adequately modeled via a circuit. The new platform introduced here will deepen the understanding of light–matter interactions and introduce even more material options to broadband metaphotonic applications, including those in integrated photonics and holographic lithography technologies.

Advanced control of light propagation is crucial for numerous modern technologies, such as high-capacity communications, optical sensing, and high-resolution imaging applications.[1–3] However, conventional optical elements are bulky and do not meet the fast-growing requirements of integration in compact systems.[4] By introducing abrupt changes in phase, amplitude, and/or polarization, metasurfaces consisting of sub-wavelength structures at an interface not only allow unprecedented control of light properties, but also enable substantial miniaturization of future photonic devices.[5,6] Versatile optical functionalities (focusing, beam steering, orbital angular momentum, hologram generation, light polarization control, and photonic spin hall effect) based on metasurfaces have been demonstrated.[7–24]

Metasurfaces based on metallic materials, such as gold (Au) and silver (Ag), have been first shown to be functional from terahertz to near-IR.[7,8,15,16,19,23] However, because of intrinsic Ohmic losses, their performance deteriorates substantially in the visible to UV regions, where a variety of ubiquitous applications are of interest (e.g., high-resolution photolithography, imaging, and chemical/biological sensing applications).[25] Aluminum (Al) has a potentially better response at shorter wavelengths,[19] but it suffers from oxidation-induced performance degradation and fabrication challenges when scaled down.[26,27] Dielectric materials, including Si, titanium dioxide (TiO_2), silicon nitride (Si_3N_4), and gallium nitride (GaN), have recently been utilized to construct efficient metasurfaces based on Mie resonances or the so-called waveguide modes at IR and visible frequencies.[9–14,17,18,20–22,24] However, such designs suffer from the materials' inter-band transitions in the UV range (e.g., TiO_2 at 3.2 eV and GaN at 3.4 eV), especially due to the resonances. Moreover, the reported thicknesses of dielectric metasurfaces were close to or even larger than their operation wavelengths, leading to challenging height-to-width ratios of 10–15.[11,13,14,18,20–22,24] In addition, most UV transparent dielectrics have low refractive indices (e.g., MgF_2, CaF_2, and SiO_2), posing more severe challenges to the metasurface design and fabrication for the UV range. Low index contrast compared to the substrates also compromises the performance. Some nanostructures are reported to manipulate light in the UV regimes,[28–31] but none of them are able to engineer wavefront.

Y. Deng, Dr. X. Wang, Z. Gong, Dr. K. Dong, S. Lou, K. B. Tom, F. Yang, Prof. J. Yao
Department of Materials Science and Engineering
University of California
Berkeley, CA 94720, USA
E-mail: yaojie@berkeley.edu

Dr. K. Dong, K. B. Tom, Prof. J. Yao
Materials Sciences Division
Lawrence Berkeley National Laboratory
Berkeley, CA 94720, USA

Dr. K. Dong, Prof. Z. You
State Key Laboratory of Precision Measurement Technology and Instruments
Department of Precision Instrument
Tsinghua University
Beijing 100084, P. R. China

Dr. N. Pégard, Prof. L. Waller
Department of Electrical Engineering and Computer Sciences
University of California
Berkeley, CA 94720, USA

Dr. N. Pégard
Department of Molecular and Cell Biology
University of California
Berkeley, CA 94720, USA

**ADVANCED
SCIENCE NEWS**

www.advancedsciencenews.com

**ADVANCED
MATERIALS**

www.advmat.de
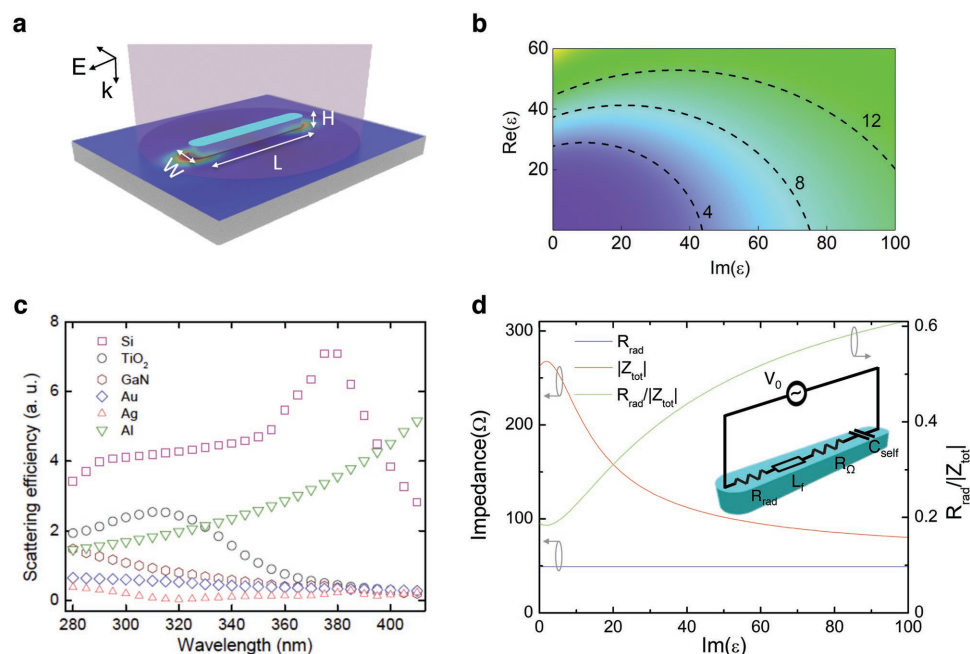
Figure 1. Circuit model for lossy dielectric nanorod and calculated scattering efficiency comparison between different materials. a) Schematic configuration of a nanorod and scattering field (there is no substrate in the circuit model calculation). b) Color mapping of scattering efficiency of a nanorod as a function of $Re(\varepsilon)$ (ε_r) and $Im(\varepsilon)$ (ε_i), with $L = 130$ nm, $W = 30$ nm, and $H = 30$ nm at the wavelength of 380 nm. c) Scattering efficiency of nanorods made of different materials, including Si, TiO$_2$, GaN, Au, Ag, and Al with the same geometric parameters. d) R_{rad}, $|Z_{tot}|$ and $R_{rad}/|Z_{tot}|$ plotted as a function of ε_i when ε_r is fixed at 10. Inset: Circuit model for a nanorod.

Here, we take a completely new route to realize broadband UV metasurfaces, which enables the manipulation of the wavefront of UV light for the first time. We show that strongly absorbing materials may serve as good candidates for UV metasurfaces, because enhancement of either the real part (ε_r) or the imaginary part (ε_i) of material permittivity effectively improves the scattering efficiency of nanoantennas, as discussed in the following section. Moreover, a large ε_i typically coexists with a large ε_r around the absorption peaks due to causality implied by the Kramers–Kronig relations.[32,33] Hence, we can take advantage of the impacts of both ε_r and ε_i on scattering efficiencies and achieve metasurfaces working at down to 290 nm wavelength, the shortest effective working wavelength for metasurfaces ever reported, to the best of our knowledge. Based on the new platform, we show photolithography using metasurface-generated UV holograms. The Si platform is naturally compatible with mature complementary metal-oxide–semiconductor (CMOS) fabrication technologies, making it practically promising and cost-effective.

Among metasurface designs, the scatterer-orientation-controlled geometric phase (Pancharatnam–Berry phase) approach has been widely utilized to manipulate the phase of the scattered field for circularly polarized light.[34,35] The same approach is used in this work to provide a benchmark in the evaluation of our broadband UV metasurfaces. A nanorod-shaped scatterer is able to control the phase of the scattered light with opposite helicity by only changing the orientation angle of the scatterer. And the phase is not subjected to variations in size and material properties, upon which the scattering efficiency is dependent.[9,11,16,18,19,21,22] This unique feature endows us with great freedom in optimizing the efficiency of the nanoantennas

without sacrificing the phase control. Here, we first investigate the scattering efficiency of a nanorod consisting of a material with arbitrary permittivities, as depicted in **Figure 1**a (the environment is air) with length (L), width (W), and height (H). Figure 1b plots the color contour of the scattering efficiency of a nanorod as a function of the ε_r and ε_i at 380 nm. Here the scattering efficiency is defined as the ratio of the scattering cross section and the cross-sectional area of the scatterer. As shown in Figure 1b, not only ε_r but also ε_i contribute positively to the scattering efficiency in a dissipative system. The scattering cross section increases substantially when ε_i becomes larger. The positive effect of ε_i on scattering efficiency can be understood on the basis that large ε_i shields the field from entering the nanorod. A drastic example would be a very large imaginary part of permittivity (in the limit of a perfect conductor), for which the antenna will have the maximized scattering efficiency. Based on the above analysis, single-crystal Si is chosen as the material platform for efficient metasurfaces, due to its large ε_i at UV frequencies, CMOS compatibility, and mature fabrication technologies (the refractive index and permittivity spectra are plotted in Figure S1, Supporting Information). To demonstrate the distinct property of Si at UV frequencies, we compare the single-nanorod scattering efficiencies of different materials (widely used for the metasurfaces), including Si, TiO$_2$, GaN, Au, Ag, and Al, over a broad range of UV wavelengths from 290 to 410 nm (Figure 1c). When the length is fixed at 130 nm (other lengths cases are discussed in Figure S2, Supporting Information), the Si nanorod outperforms all others, demonstrating the effectiveness of Si nanoantennas in the UV range.

In order to better understand the light–matter interaction here, especially the quantitative behavior of the influence of

**ADVANCED
SCIENCE NEWS**

www.advancedsciencenews.com

**ADVANCED
MATERIALS**

www.advmat.de
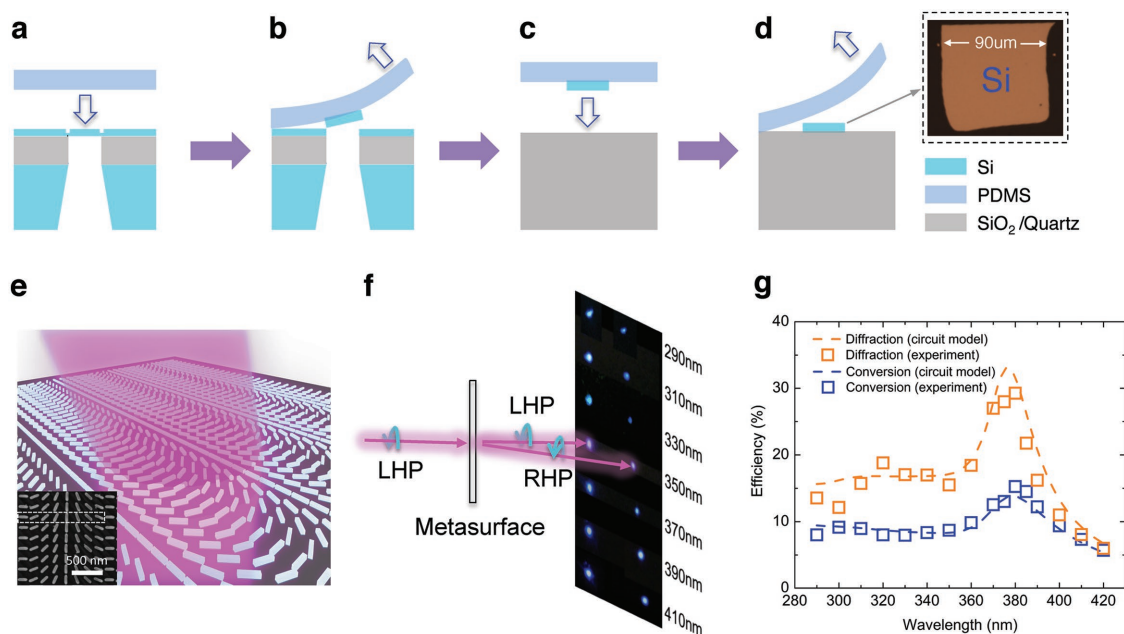
Figure 2. Design, fabrication, and characterization of the metasurface for beam steering. a–d) Si membrane transfer process with a PDMS stamp. Inset of (d): optical image of a piece of transferred Si membrane on quartz substrate. e) Schematic of the metasurface and its building blocks, Si nanorods lying on a quartz substrate, with unit dimensions $a_x \times a_y$ ($a_x = a_y$, period of a single unit, 160 nm in the design). Inset: SEM picture of the metasurface for beam steering. Eight periods form a unit cell covering 2π phase shift (labeled as white dashed box). f) Optical image of the unconverted and bent beams on a luminescent screen for wavelengths from 290 to 410 nm. LHP: left-hand polarization; RHP: right-hand polarization. g) Theoretically calculated (with circuit model; dashed line), and experimentally measured (cubic scatterers) conversion efficiency and diffraction efficiency of the metasurface. Fabricated nanorod dimensions: $L = 142$ nm, $W = 32$ nm, and $H = 35$ nm. The optimization of geometric parameters (L, W, H, and period) is obtained with simulations while taking into account the possible fabrication challenges.

material permittivity on the scattering efficiency, we construct a circuit model to calculate the scattering efficiency of a nanorod (inset of Figure 1d).[36] The circuit contains an AC voltage source (V_0) that models the incident plane wave. The total impedance (Z_{tot}) of a nano-antenna includes radiation resistance (R_{rad}), self-inductance in the rod (L_f), Ohmic resistance (R_Ω) and self-capacitance (C_{self}) in dielectric materials. The capacitance in the air is parallel to the voltage source, so that it does not affect the calculation. The R_{rad} is independent of material permittivities;[37] the energy "lost" to R_{rad} is the scattered energy. The detailed model and expressions of the circuit elements can be found in Section S3 (Supporting Information). Figure 1d indicates that increasing ε_i reduces $|Z_{tot}|$ of the circuit while the R_{rad}, is a constant (see Section S3, Supporting Information). Similar behavior was theoretically discussed previously.[38] In addition to the large permittivity induced high scattering efficiency, the circuit model also allows for understanding of more details behind. As shown in Figure 1c, there are two peaks in scattering efficiency spectrum of Si antenna. One is around 380 nm, which is a result of resonance. The other peak close to 300 nm is due to low impedance of Si antenna. More detailed discussions are provided in Section S3 (Supporting Information).

This large permittivity-induced high scattering efficiency enables us to utilize common lossy dielectrics to realize metasurfaces over a broad range, including the UV region. To experimentally demonstrate the effectiveness of the single-crystal Si platform in the UV range, we design, fabricate, and characterize all-Si metasurfaces for two typical applications: UV beam steering and holographic lithography. Note that our

new platform is highly versatile and can be used in many other applications as well.

The single-crystal Si is obtained by transferring a suspended Si membrane from a transmission electron microscope (TEM) grid (SiMPore Inc.) to a quartz substrate with a poly(dimethylsiloxane) (PDMS) stamp, as illustrated in **Figure 2**a–d (see details in the Experimental Section, Supporting Information).[39] The size of the transferred single-crystal Si is approximately 90 µm × 90 µm. The inset of Figure 2d shows an optical image of a transferred Si membrane on a quartz substrate. Along with refractive index and permittivity spectra, an electron diffraction pattern of the Si membrane is shown in Figure S1c (Supporting Information), confirming its single crystallinity.

In the demonstration of UV beam steering, each unit cell of the metasurface (labeled as a dashed box in inset of Figure 2e) is composed of eight optimized Si nanorods with different orientation angles lying on a quartz substrate, as illustrated in Figure 2e (each nanorod is in a single unit). The inset of Figure 2e shows the scanning electron microscopy (SEM) image of the fabricated metasurface for the beam steering (see Experimental Section). The unit cell covers 2π phase shift, leading to a bending angle of approximately 13.1 degrees at 290 nm wavelength and 17.3 degrees at 380 nm, as shown in Figure 2f and Figure S5c (Supporting Information). The measured bending angles for different wavelengths follow the theory well (see Figure S5c, Supporting Information). The conversion efficiency (the ratio of the power of the bent beam to the total incident power) and diffraction efficiency (the ratio of the power of the bent beam to the direct transmitted power[40]) are measured using the

**ADVANCED
SCIENCE NEWS**

www.advancedsciencenews.com

**ADVANCED
MATERIALS**

www.advmat.de
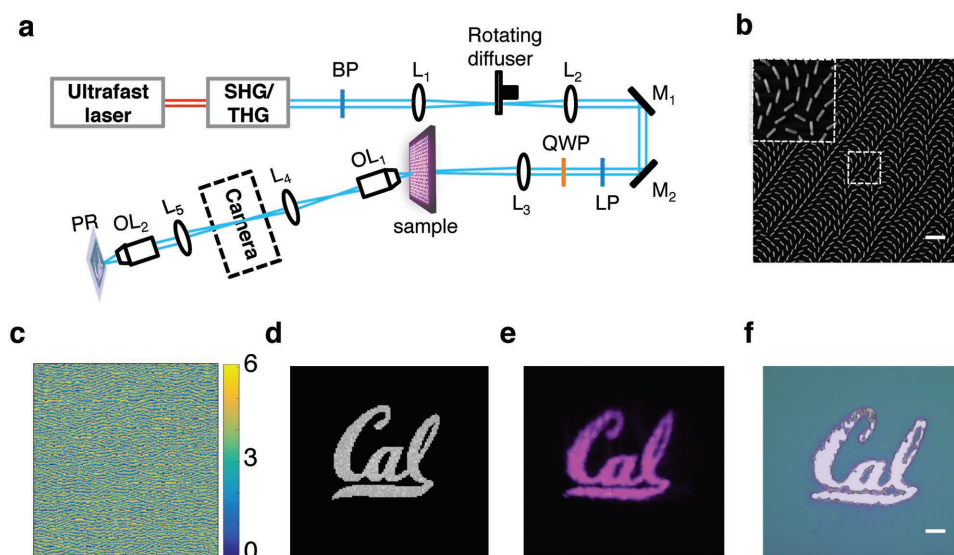
Figure 3. UV hologram for arbitrary patterns. a) Experimental setup for photolithography enabled by generated hologram. Abbreviations used for the optical components are as follows. BP: band pass filter; L_1, L_2, L_3, L_4, L_5: lenses; M_1, M_2: mirrors; LP: linear polarizer; QWP: quarter wave plate; OL_1, OL_2: objective lenses; PR: photoresist (S1805). The camera is removed during the exposure. b) SEM microimage of the fabricated metasurfaces for "Cal" pattern hologram. The inset shows the magnified image of the nanorods in the white dashed box. Scale bar: 500 nm. c) Phase distribution of target image ("Cal" logo) obtained with the algorithm mentioned above and d) theoretically calculated holographic "Cal" pattern based on the phase distribution in (c). e) Camera-captured holographic "Cal" pattern. The operating wavelength is 380 nm. f) "Cal" pattern exposed on photoresist. Scale bar: 10 μm.

experimental setup shown in Figure S4 (Supporting Information). Over a broadband range from 290 to 410 nm, the conversion efficiency reaches as high as 15% at 380 nm and remains at the level of 10% even at the short wavelength of 290 nm. Meanwhile, the diffraction efficiency achieves 30% around 380 nm and maintains over 15% at shorter wavelengths. The experimental results plotted in Figure 2g are in good agreement with circuit model calculations, which are plotted as dashed curves in the same figure (Figure 2g). Further finite element method (FEM) simulation shows that the maximum efficiency in the UV range increases to 70% in the reflection mode (Figure S5e, Supporting Information). With optimization of the antenna design, even higher efficiencies for both transmission and reflection modes can be achieved. For example, by introducing a double-bar design (Supporting Information S6, Supporting Information), the efficiency of the all-Si metasurface can be increased to the level of 200% (diffraction efficiency) and 37% (conversion efficiency) in the transmission mode. This high diffraction efficiency will be essential to improve the signal-to-noise ratio in the far field transmission. Moreover, the mechanism we propose here is not limited to Si only. Any material that possesses a large permittivity may have strong scattering capability and materials with larger permittivity than that of Si will enable higher efficiency metasurfaces than Si ones with similar structures. The demonstration of effective UV beam steering successfully confirms the proposed mechanism that the scattering efficiency of nano-optic antennas benefits substantially from the strong interaction between Si and UV light.

The high photon energies and short wavelengths of UV light are highly favorable for photolithography applications. Even 3D lithography of periodic structures has been achieved with UV illumination.[41] Here, for the first time to the best of our knowledge, we demonstrate metasurface-based holographic

lithography of arbitrary patterns. The manipulation of phase for each individual antenna of a metasurface allows the implementation of computer-generated holography. Our setup is demonstrated at 380 nm, close to the widely used mercury *i*-line. The 380 nm wavelength was chosen simply for the convenience of measurement. Much shorter working wavelengths can be used if needed. The example hologram we create here is a "Cal" logo. The discrete phase distribution (32 phase levels covering 2π) is generated by an iterative nonlinear optimization algorithm that provides improved quality over the traditional Gerchberg–Saxton method by exploiting the binary nature of the target pattern,[42] as shown in **Figure 3c** (for target image "Cal" logo pattern). The calculated pattern of the "Cal" logo is shown in Figure 3d. Figure 3b shows a high-resolution SEM image of the fabricated metasurface for target "Cal" logo. The experimental setup is depicted in Figure 3a, where speckle noise is reduced by a 4f system (L_1 and L_2) with a diffuser in the illumination path. The rotating diffuser is placed at the Fourier plane, which reduces temporal coherence while maintaining spatial coherence. A camera is used to capture the image of "Cal" logo pattern (Figure 3e), and then a demagnified pattern exposes the photoresist (Figure 3f). All features shown in Figure 3e, including the uneven boundaries and all fine features, are transferred to the resist (Figure 3f), confirming the high fidelity of the lithography process. Our approach allows the generation of arbitrary holographic patterns with fine features down to the diffraction limit. A unique advantage of UV holography is that its high photon energies and short wavelengths have great potential for more advanced applications; for example, a single 2D mask can generate multiple holographic patterns at the same time, each at a different image plane, enabling high-throughput fabrication and the potential for 3D lithography, a step forward from existing lithography technologies.[37]

ADVANCED
SCIENCE NEWS

www.advancedsciencenews.com

ADVANCED
MATERIALS

www.advmat.de

Utilizing the all-single-crystal Si platform, we have experimentally demonstrated broadband UV metasurfaces working efficiently at wavelengths down to 290 nm. The FEM simulation predicts 70% conversion efficiency in the reflection mode beam steering. A double-bar structure design is proposed to improve the diffraction efficiency to around 100% in transmission mode over a broad UV band. A circuit model is built which accurately describes the total impedance modulation by the material permittivity. Enabled by the new capability in manipulating UV light, we have achieved holographic lithography of arbitrary patterns. The Si platform is naturally compatible with mature CMOS fabrication technologies, making it practically promising and cost-effective. By employing other larger bandgap materials, the working spectrum range can be even broadened to far-UV frequencies. Moreover, this metasurface-based lithography can be potentially extended to 3D with 3D holography, providing new opportunities for future nanomanufacturing.

Experimental Section

Silicon Membrane Transfer and Metasurface Fabrication Processes: The fabrication process of all-Si metasurfaces begins with the transfer of a single-crystal silicon membrane onto a quartz substrate using a PDMS stamp. The silicon membrane was obtained from a commercially available TEM grid (SiMPore Inc., US100-C35Q33). First of all, a metallic probe was used to break the Si windows on TEM grid. A PDMS (Sylgard 184 Silicone elastomer, Dow Corning) stamp, which was mounted on a micromanipulator, was attached to the heated TEM grid windows (suspended Si membrane) ($\approx$60 °C). As the PDMS was transparent, the Si membrane can be seen under the microscope. Once it cools down to the room temperature, the Si membrane with the PDMS was peeled off the TEM grid. The Si membrane can be identified on the PDMS. Then, a heated acceptor substrate (quartz) ($\approx$60 °C) was fixed on a XYZ stage. The PDMS stamp was then attached and pressed against the surface of the quartz substrate. The substrate temperature was then increased to 90 °C to improve the adhesion of Si membrane to the quartz substrate. Finally, it was peeled off very slowly at 90 °C, resulting in the Si membrane attaching well to the quartz substrate via Van de waals force. As the stamp was transparent, one can see the Si membrane through it and thereby it was possible to align the Si membrane to the desired location on both the PDMS and the acceptor substrate. The electron diffraction pattern from the silicon membrane is shown in Figure S1c (Supporting Information), confirming that it was indeed single crystal.

Electron beam lithography and standard reactive etching (HBr/Cl$_2$) techniques were utilized to fabricate the metasurface patterns on the silicon film. Electron beam resist, hydrogen silsesquioxane was used in the lithography. It was not removed finally since it does not affect the performance of the metasurface.

Optical Setup for Measuring the Conversion Efficiency Spectra: The optical setup for measuring the conversion efficiency spectra is depicted in Figure S4 (Supporting Information). A femto-second laser (Coherent, Chameleon Ultra II) combined with a tripler (Coherent, Chameleon second-harmonic generation (SHG)/third-harmonic generation (THG)), which can generate coherent UV light source from 228 to 500 nm, was used. In the measurement, SHG covers the wavelength range from 340 to 410 nm while THG provides 290 to 340 nm light. A polarizer (Thorlabs, GLB10) and a quarter-wave plate (Thorlabs, AQWP05M-340) were employed to generate the wavefront (circular polarization) required by the metasurface. The optical powers of the bent beam and the incident beam were captured by a photodetector (Conherent, Controller: FieldMaxII-TO Laser Power Meter; head: OP-2UV). A

luminescent screen after the metasurface captures the beam spots (unconverted and converted beams). The distance between those two beam spots and the one between the luminescent screen and the metasurface were measured to calculate the bending angle, as shown in Figure S5b,c (Supporting Information). The theoretical value of the bending angle (θ) was determined by (shown in Figure S5a, Supporting Information)

$$\theta = \sin^{-1}\left(\frac{\lambda}{8a}\right)$$

where $a = a_x = a_y$ (single unit period), which was 160 nm. The bending angle can be varied by changing the unit cell size (phase levels to cover 2π phase shift, which was eight in the design for beam bending) and a. With a similar design for metasurface but with a spacer layer and Al mirror, FEM simulations demonstrate that the Si metasurface efficiency in the UV can reach up to 70% in the reflection mode, as shown in Figure S5D,E (Supporting Information).

Optical Setup for Hologram-Enabled Lithography Experiment: For holographic lithography, an off-axis design was applied such that the image propagates in the similar way as the bent beam (Figure S5a, Supporting Information). As discussed above, a 4f system was inserted in the illumination path and a rotating diffuser (Edmund, #47989) in the focused beam plane to reduce the laser speckle noise. After the metasurface, a Mitutoyo long-working-distance objective lens (M Plan Apo SL100×, NA = 0.55; working distance = 13 mm; effective focal length = 2 mm) and a fused silica lens (focal length = 38 mm) were used to form an image of holographic "Cal" pattern on a CMOS camera (Thorlabs, DCC1645C). Another two-lens system consisting of a fused silica lens (focal length = 200 mm) and a Mitutoyo objective lens (M Plan Apo NIR20×, NA = 0.40; working distance = 20.0 mm; effective focal length = 10 mm) were employed to shrink the size of the image by 20 times and the image was then recorded by the photoresist (S1805). Photoresist S1805 was spin-coated with a speed of 5000 rpm, forming a thickness of around 400 nm and it was developed with MF-319 developer (MicroChem).

Supporting Information

Supporting Information is available from the Wiley Online Library or from the author.

Acknowledgements

Conflict of Interest

The authors declare no conflict of interest.

Keywords

1802632 (5 of 6)

**ADVANCED
SCIENCE NEWS**

www.advancedsciencenews.com

**ADVANCED
MATERIALS**

www.advmat.de

[1]   Y. Yan, G. Xie, M. P. J. Lavery, H. Huang, N. Ahmed, C. Bao, Y. Ren, Y. Cao, L. Li, Z. Zhao, A. F. Molisch, M. Tur, M. J. Padgett, A. E. Willner, *Nat. Commun.* **2014**, *5*, 4876.

[2]   K. V. Sreekanth, Y. Alapan, M. ElKabbash, E. Ilker, M. Hinczewski, U. A. Gurkan, A. De Luca, G. Strangi, *Nat. Mater.* **2016**, *15*, 621.

[3]   N. Fang, H. Lee, C. Sun, X. Zhang, *Science* **2005**, *308*, 534.

[4]   G. Lifante, *Integrated Photonics: Fundamentals*, J. Wiley, Hoboken, NJ **2003**.

[5]   N. Yu, F. Capasso, *Nat. Mater.* **2014**, *13*, 139.

[6]   A. V. Kildishev, A. Boltasseva, V. M. Shalaev, *Science* **2013**, *339*, 1232009.

[7]   N. Yu, P. Genevet, M. A. Kats, F. Aieta, J. P. Tetienne, F. Capasso, Z. Gaburro, *Science* **2011**, *334*, 333.

[8]   X. Ni, N. K. Emani, A. V. Kildishev, A. Boltasseva, V. M. Shalaev, *Science* **2012**, *335*, 427.

[9]   D. Lin, P. Fan, E. Hasman, M. L. Brongersma, *Science* **2014**, *345*, 298.

[10] F. Monticone, N. M. Estakhri, A. Alù, *Phys. Rev. Lett.* **2013**, *110*, 203903.

[11] M. Khorasaninejad, W. T. Chen, R. C. Devlin, J. Oh, A. Y. Zhu, F. Capasso, *Science* **2016**, *352*, 1190.

[12] M. Khorasaninejad, F. Capasso, *Science* **2017**, *358*, eaam8100.

[13] A. Amir, Y. Horie, M. Bagheri, A. Faraon, *Nat. Nanotechnol.* **2015**, *10*, 937.

[14] A. Zhan, S. Colburn, R. Trivedi, T. K. Fryett, C. M. Dodson, A. Majumdar, *ACS Photonics* **2016**, *3*, 209.

[15] J. Lin, P. Genevet, M. A. Kats, N. Antoniou, F. Capasso, *Nano Lett.* **2013**, *13*, 4269.

[16] G. Zheng, H. Mühlenbernd, M. Kenney, G. Li, T. Zentgraf, S. Zhang, *Nat. Nanotechnol.* **2015**, *10*, 308.

[17] Y. Yang, W. Wang, P. Moitra, I. I. Kravchenko, D. P. Briggs, J. Valentine, *Nano Lett.* **2014**, *14*, 1394.

[18] R. C. Devlin, A. Ambrosio, N. A. Rubin, J. P. B. Mueller, F. Capasso, *Science* **2017**, *358*, 896.

[19] P. C. Wu, W. Y. Tsai, W. T. Chen, Y. W. Huang, T. Y. Chen, J. W. Chen, C. Y. Liao, C. H. Chu, G. Sun, D. P. Tsai, *Nano Lett.* **2016**, *17*, 445.

[20] W. T. Chen, A. Y. Zhu, V. Sanjeev, M. Khorasaninejad, Z. Shi, E. Lee, F. Capasso, *Nat. Nanotechnol.* **2018**, *13*, 220.

[21] S. Wang, P. C. Wu, V. C. Su, Y. C. Lai, M. K. Chen, H. Y. Kuo, B. H. Chen, Y. H. Chen, T. T. Huang, J. H. Wang, R. M. Lin, C. H. Kuan, T. Li, Z. Wang, S. Zhu, D. P. Tsai, *Nat. Nanotechnol.* **2018**, *13*, 227.

[22] B. H. Chen, P. C. Wu, V. C. Su, Y. C. Lai, C. H. Chu, I. C. Lee, J. W. Chen, Y. H. Chen, Y. C. Lan, C. H. Kuan, D. P. Tsai, *Nano Lett.* **2017**, *17*, 6345.

[23] X. Yin, Z. Ye, J. Rho, Y. Wang, X. Zhang, *Science* **2013**, *339*, 1405.

[24] Z. Shi, M. Khorasaninejad, Y. W. Huang, C. Roques-Carmes, A. Y. Zhu, W. T. Chen, V. Sanjeev, Z. W. Ding, M. Tamagnone, K. Chaudhary, R. C. Devlin, C. W. Qiu, F. Capasso, *Nano Lett.* **2018**, *18*, 2420.

[25] J. R. Bolton, *Ultraviolet Applications Handbook*, Bolton Photosciences Inc., Edmonton, AB, Canada **2001**.

[26] M. W. Knight, N. S. King, L. Liu, H. O. Everitt, P. Nordlander, N. J. Halas, *ACS Nano* **2013**, *8*, 834.

[27] J. Martin, J. Plain, *J. Phys. D: Appl. Phys.* **2015**, *48*, 184002.

[28] C. Argyropoulos, F. Monticone, G. D'Aguanno, A. Alù, *Appl. Phys. Lett.* **2013**, *103*, 143113.

[29] S. V. Makarov, A. N. Tsypkin, T. A. Voytova, V. A. Milichko, I. S. Mukhin, A. V. Yulin, S. E. Putilin, M. A. Baranov, M. A. A. E. Krasnok, I. A. Morozov, P. A. Belov, *Nanoscale* **2016**, *8*, 17809.

[30] K. Liu, S. Jiang, D. Ji, X. Zeng, N. Zhang, H. Song, Y. Xu, Q. Gan, *IEEE Photonics Technol. Lett.* **2015**, *27*, 1539.

[31] A. Soni, S. Purohit, R. S. Hegde, *IEEE Photonics Technol. Lett.* **2017**, *29*, 110.

[32] R. de L. Kronig, *J. Opt. Soc. Am.* **1926**, *12*, 547.

[33] H. A. Kramers, *Atti Cong. Intern. Fisici (Trans. Volta Centenary Congress) Como.* **1927**, *2*, 545.

[34] M. V. Berry, *J. Mod. Opt.* **1987**, *34*, 1401.

[35] S. Pancharatnam, *Proc. Indian Acad. Sci., Section A* **1956**, *44*, 398.

[36] M. Eggleston, K. Messer, L. Zhang, E. Yablonovitch, M. Wu, *Proc. Natl. Acad. Sci.* **2015**, *112*, 1704.

[37] C. A. Balanis, *Antenna Theory: Analysis and Design*, 4th ed., John Wiley and Sons, Hoboken, NJ **2016**.

[38] R. Fleury, J. Soric, A. Alù, *Phys. Rev. A* **2014**, *89*, 045122.

[39] K. S. Kim, Y. Zhao, H. Jang, S. Y. Lee, J. M. Kim, K. S. Kim, J. H. Ahn, P. Kim, J. Y. Choi, B. H. Hong, *Nature* **2009**, *457*, 706.

[40] F. Qin, L. Ding, L. Zhang, F. Monticone, C. C. Chum, J. Deng, S. Mei, Y. Li, J. Teng, M. Hong, S. Zhang, *Sci. Adv.* **2016**, *2*, 1.

[41] M. Campbell, D. N. Sharp, M. T. Harrison, R. G. Denning, A. J. Turberfield, *Nature* **2000**, *404*, 53.

[42] J. Zhang, N. Pégard, J. Zhong, H. Adesnik, L. Waller, *Optica* **2017**, *4*, 1306.

1802632 (6 of 6)